



HAL
open science

Simplified tomographic diffractive microscopy for axisymmetric samples

Ludovic Foucault, Nicolas Verrier, Matthieu Debailleul, Bertrand Simon,
Olivier Haerberle

► **To cite this version:**

Ludovic Foucault, Nicolas Verrier, Matthieu Debailleul, Bertrand Simon, Olivier Haerberle. Simplified tomographic diffractive microscopy for axisymmetric samples. *OSA Continuum*, 2019, 2 (4), pp.1039-1055. 10.1364/OSAC.2.001039 . hal-03615860

HAL Id: hal-03615860

<https://hal.science/hal-03615860>

Submitted on 21 Mar 2022

HAL is a multi-disciplinary open access archive for the deposit and dissemination of scientific research documents, whether they are published or not. The documents may come from teaching and research institutions in France or abroad, or from public or private research centers.

L'archive ouverte pluridisciplinaire **HAL**, est destinée au dépôt et à la diffusion de documents scientifiques de niveau recherche, publiés ou non, émanant des établissements d'enseignement et de recherche français ou étrangers, des laboratoires publics ou privés.

Simplified tomographic diffractive microscopy for axisymmetric samples

LUDOVIC FOUCAULT,¹ NICOLAS VERRIER,¹ MATTHIEU DEBAILLEUL,¹ BERTRAND SIMON,² OLIVIER HAEBERLÉ^{1,*}

¹*Institut de Recherche en Informatique, Mathématiques, Automatique et Signal (IRIMAS EA7499), Université de Haute-Alsace, 61 rue Albert Camus, 68093 Mulhouse Cedex, France*

²*Laboratoire Photonique Numérique et Nanoscience (LP2N), CNRS UMR5298, Université de Bordeaux, Institut d'Optique Graduate School, Talence 33405, France*

**olivier.haeberle@uha.fr*

Abstract: Tomographic diffractive microscopy exhibits intrinsic features making it a method of choice for 3D high-resolution label-free imaging. However, these results are achieved at the cost of a heavy data acquisition/reconstruction process. This drawback can be circumvented for certain class of samples. For example, axisymmetric samples, like optical or textile fibers, present geometrical properties that can be advantageously used to speed-up the acquisition process. We propose to take benefit of these properties to allow for full reconstruction of axisymmetric samples' complex refractive index distribution, using four approaches, adapted to 3D samples. We applied the proposed reconstruction scheme, based on a numerical rotation of data, to both simulated and experimental data sets.

© 2019 Optical Society of America under the terms of the [OSA Open Access Publishing Agreement](#)

1. Introduction

For the last decades, several non-destructive techniques have been used for quality control purposes [1, 2]. Among these procedures, optical techniques have been particularly useful to reconstruct natural and optical fibers [3–8]. For instance, interferometric techniques such as Digital Holographic Microscopy (DHM) have been used, with the benefit of recording the complex field, *i.e.* both amplitude and phase images [9, 10].

In interferometric microscopy, information about the investigated medium is encoded in an interferogram allowing for extraction of either amplitude or phase contrast, in a three-dimensional volume, without the need of fluorescent dye [11–18]. This is namely the case of DHM, which, coupled with data processing, allows reconstruction of a 3D complex volume from only one recording [19, 20]. However, due to the fact that the complex field is reconstructed using a single 2D image, resolution along the light propagation axis is very limited [21].

Full 3D reconstruction has been demonstrated in the framework of Tomographic Diffractive Microscopy (TDM), which is an extension of DHM. In transmission regime, lateral resolution down to $\lambda/3.5NA$ has been demonstrated [13]. To achieve full 3D reconstruction, the investigated object is observed from several illumination directions. This can be done either by sequentially varying the illumination angle or by rotating the imaged sample [22–25]. However, both methods exhibit a lack of spatial frequencies, resulting in a resolution loss. One way to alleviate this issue is to combine illumination angle sweeping with sample rotation [26], allowing for improved isotropic resolution without sample labelling [18].

When axisymmetric samples are considered, acquiring the full set of tomographic acquisition is not mandatory, and 3D refractive index distribution reconstruction can be performed through a single acquisition [27]. It is hereby demonstrated that, considering axial symmetry of the sample, inverse Abel transform [28] allows for reconstructing 3D refractive index distribution from a single acquisition. This might be a method of choice for reducing data acquisition load [29], while keeping a true 3D reconstructed information. However, this method can only be applied to

either pure phase or pure amplitude objects, and does not account for diffraction, which limits its accuracy.

Based on the intrinsic capabilities of TDM, we propose a reconstruction framework, accounting for diffraction and allowing for complete 3D reconstruction of refractive index distribution from a single holographic or tomographic acquisition. We will first describe our TDM acquisition scheme. Then the proposed reconstruction methods are applied to simulated data when axisymmetric samples are considered. Robustness of the proposed methods is then discussed. Finally, benefits of the proposed schemes is applied on experimental data.

2. Tomographic Diffractive Microscopy principles

DHM allows for extraction of both amplitude and phase information either through spatial [30] or temporal phase [31, 32] modulation/demodulation. TDM can be considered as an extension of DHM [33–35], allowing for a full control of the object illumination angle. A schematic view of our TDM configuration is given by Fig. 1.

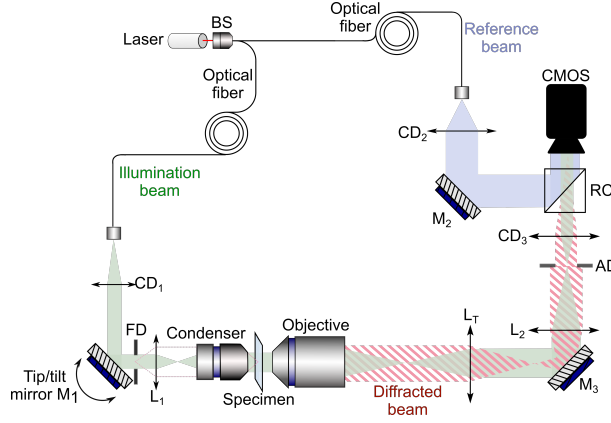


Fig. 1: Schematic representation of the TDM set-up. BS: beam splitter; CD₁, CD₂ and CD₃: collimating doublets; FD: field diaphragm; L₁: scanning lens; L_T: tube lens; AD: aperture diaphragm; RC: recombination cube; M₂ and M₃: mirrors. L₂ and CD₃ are used for sampling purposes.

The light source (475 nm DPSS B&W Tek BWB-475-10-OEM) is split into two beams with a fiber-based beam splitter. One beam is used as an interferometric reference (depicted in green in Fig. 1), while the other is used for the object illumination (in blue). Full control of the illumination beam is brought by the use of a fast tip/tilt mirror (Newport[®] FSM-300). The illumination is then focused using a $\times 100$ NA = 1.4 oil immersion Olympus[®] objective as a condenser, and diffracted by the object (in red stripes). The diffracted wave is collected through the objective ($\times 100$ NA = 1.4 oil immersion Olympus[®]), collimated using a tube lens, resized and filtered with a telecentric system. Finally, for each illumination angle, an interference pattern between the reference beam and the beam diffracted by the object is generated using a recombination cube and recorded onto a CMOS camera (PHF-MV1-D2048-96-G2 PhotonFocus[®]). Typically, a tomographic acquisition consists in the recording of tens to hundreds of holograms, recorded at various illumination angles [13]. Then, amplitude and phase can be straightforwardly retrieved via spatial demodulation of the acquired hologram stack [30]. Under the first Born approximation, we have

$$\mathbf{k}_0 = \mathbf{k}_d - \mathbf{k}_i, \quad (1)$$

with \mathbf{k}_0 the object vector potential, \mathbf{k}_i the illumination vector and \mathbf{k}_d the diffracted vector [34].

The light diffracted by the sample maps the Ewald sphere [35]. Light collection being realized through a microscope objective with limited numerical aperture, only a cap of sphere is mapped, which radius is linked to the wavelength in the propagating medium. The aim of TDM is to collect a sufficient amount of caps so that the Fourier space is adequately filled [36].

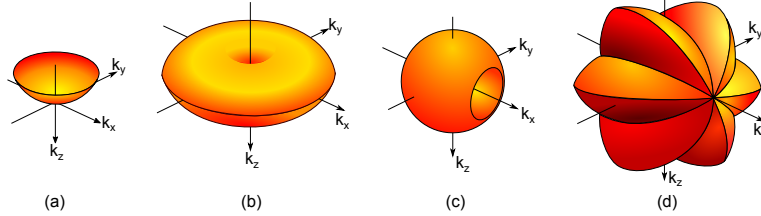


Fig. 2: (a) **Optical Transfer Function (OTF) in a simple holographic transmission setup.** (b) OTF in TDM with illumination rotation (note the “missing cone” along the optical axis). (c) OTF in TDM with sample rotation (note the “missing apple core” along k_x). (d) OTF for a combination of illumination and sample rotation approaches (0° , 60° and 120°).

Optical Transfer Functions (OTF) are presented Fig. 2 for DHM (Fig. 2(a)), TDM with illumination rotation (Fig. 2(b)), TDM with sample rotation (Fig. 2(c)) and TDM combining both approaches (Fig. 2(d)). For illumination rotation, spatial frequency extension along $k_{x,y}$ is doubled compared to classical holographic experiments. However, because of the so-called “missing cone”, no frequency along k_z can be captured [13,37]. In other words, axial resolution of TDM with illumination rotation is very limited. As noticed from Fig. 2(c), when sample rotation is considered, frequency content is degraded along the sample’s rotation axis (k_x frequency component in that case) [38]. Finally, by combining sample rotation with illumination rotation for each sample angular position, it is possible to obtain the OTF depicted Fig. 2(d). Here, 3D accessible resolution is isotropic [18,26]. From these constructed 3D spectra, the complex 3D information about the sample’s permittivity is obtained applying an inverse three-dimensional Fourier transform. Accuracy of the reconstruction and achievable resolution are therefore closely linked to the acquisition method (see Fig. 2). For instance, to obtain an accurate reconstruction considering illumination rotation tens to hundreds of acquisition are needed. Also, for sample rotation, several tens [24] to hundreds [39] rotation angles are needed. Moreover, quality of the reconstruction is highly dependent on the accuracy of the view to view registration. Combining both schemes leads to several hundreds of acquisition per sample angular position [18,40], which can become prohibitive for routine sample characterization.

This complicated characterization can be alleviated for certain classes of sample. In the next section, we consider the case of samples, which exhibit axial symmetry. Exploiting this symmetry permits to dramatically reduce the acquisition load.

3. Simplification of acquisition: application to axisymmetric samples

3.1. Limitation of the Abel inverse transform

As stated in Sec. 2, TDM can lead to an accurate reconstruction with an almost isotropic resolution. However, the higher the targeted image quality, the longer the acquisition time. In order to be able to use TDM for routine characterization, a trade-off between acquisition speed and resolution has to be considered. For certain classes of samples, we can reduce the amount of acquired holograms while maintaining the same resolution as for one complete TDM acquisition. For example, axial-symmetry coupled with an adapted reconstruction scheme allows for reconstructing 3D refractive index distribution from a unique holographic acquisition (for cylindrical samples) or a single tomographic acquisition (for axisymmetric samples but not invariant along their axis of symmetry).

Use of single shot interferometric techniques for reconstruction of 3D refractive index profiles have been discussed for example in [27]. The proposed method, based on the Abel transform and its inversion [28], has been successfully applied to the characterization of axisymmetric jets. It relies on the fact that, for a transparent sample with axial symmetry, and considering light propagation along z axis, the reconstructed phase $\varphi(x, y)$ is linked to the refractive index of the sample by the line integral

$$\varphi(x, y) = \int_{-z_0/2}^{z_0/2} \frac{2\pi}{\lambda} \Delta n(r, y) dz, \quad (2)$$

where $\Delta n(r, y)$ is the refractive index difference between the object index $n(r, y)$ and the immersion medium refractive index n_{im} , and z_0 is the thickness of the axisymmetric object. The radial coordinate r is defined by $r = \sqrt{x^2 + z^2}$. Integral presented Eq. (2) is the Abel transform linking the refractive index distribution $\Delta n(r, y)$ to the reconstructed phase $\varphi(x, y)$. From Eq. (2), it is possible to retrieve the 3D refractive index distribution calculating the inverse Abel transform of the reconstructed phase distribution $\varphi(x, y)$

$$n(r, y) = n_{im} + \frac{\lambda}{2\pi^2} \int_r^R \left[\frac{\partial \varphi(x, y)}{\partial x} \right] \frac{dx}{\sqrt{x^2 - r^2}}, \quad (3)$$

with R being an arbitrary maximal value for the radius r . Computing Eq. (3) makes it possible to retrieve 3D information about refractive index of the investigated sample. However, this method is limited to pure phase object, as absorption is not taken into account in the model. If one has to measure absorption only, an inverse transform based on the Beer-Lambert law can be used [41]. This approach has also been proven to be quite efficient with strongly refracting phase objects [42]. However, the main drawback is that these methods can only be used for either pure amplitude or pure phase phase objects, and do not account for diffraction, which prevents them for being used for microscopic samples presenting absorption and refraction properties.

3.2. Accounting for diffraction

In order to take benefit of axisymmetry while accounting for diffraction, we developed two alternative schemes, depicted in Fig. 3, which are based on a numerical rotation of data. For axisymmetric objects, spectral content of the acquired hologram (after spatial demodulation) maps a spherical cap in the 3D Fourier space (red cap in Fig. 3(a)). Therefore, only a limited portion of the object spectrum is acquired. Nevertheless, as in such case rotating the sample is mathematically equivalent to a rotation of its 3D Fourier spectrum, it is possible to retrieve a more complete information [43]. Doing so enables reconstruction of the spectrum that one would have obtained if a real physical sample rotation was realized (see Fig. 2(c)), with the main advantage of both simplifying acquisition process and reducing the acquisition time.

Based on the projection-slice theorem, the rotation equivalency can be mathematically written as (p. 37 in [44] and adapted to our 3D problem)

$$\text{FT}\{g(x', y', z')\} = G(f_x, f_y \cos \theta + f_z \sin \theta, -f_y \sin \theta + f_z \cos \theta), \quad (4)$$

where FT designates the Fourier Transform operation, g is the object function, G its Fourier transform, θ the rotation angle in relation to the x axis, (x', y', z') the rotated Cartesian coordinates and $(f_x, f_y, f_z) = (k_x, k_y, k_z)/2\pi$ the frequencies corresponding to the initial coordinates (x, y, z) . This equation corresponds to a rotation made in the Fourier space, hence we called this approach FINER (Fourier Image NumERical Rotation) method. It can be noticed that there exists a dual equation, which can be written as

$$G(f'_x, f'_y, f'_z) = \text{FT}\{g(x, y \cos \theta + z \sin \theta, -y \sin \theta + z \cos \theta)\}, \quad (5)$$

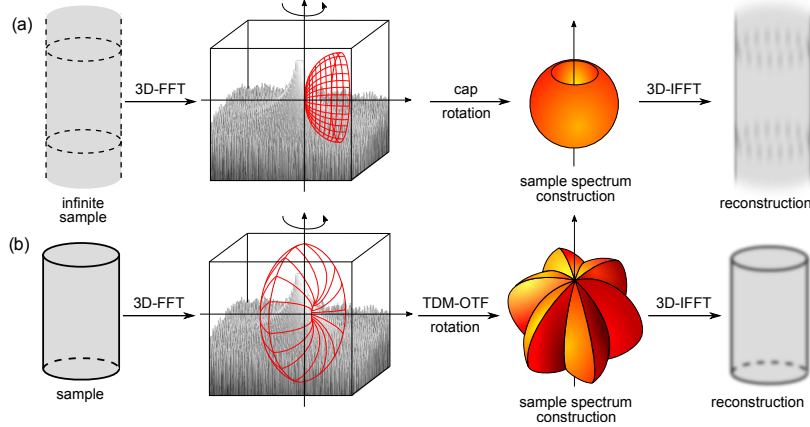


Fig. 3: Synoptics of the simulated data acquisition/reconstruction procedures of (a) FINER/DINER methods (applied to infinite samples) and (b) TINER/F-TINER method (applied to finite samples).

where (f'_x, f'_y, f'_z) are the frequencies rotated by the θ angle. It corresponds to a rotation made in the image space; we called this approach DINER (DHM Image NumERical Rotation) method.

However, applying the numerical rotation of data (in either space) based on a single cap of sphere leads to a specific shape of the frequency support (Fig. 2(c)), displaying a typical lack of frequencies (“missing apple core”) along the rotation axis [38, 45]. Hence, as depicted Fig. 3(b), a prior illumination rotation is performed, filling the Fourier space as in Fig. 2(b), thus allowing for better resolution along the rotation axis. This step is then followed by a numerical rotation of the support, as indicated in Fig. 2(d), so a resolution improvement along the k_z axis can be achieved. We called these approaches TINER (TDM Image NumERical Rotation, rotation in image space) and F-TINER (rotation in Fourier space) methods. In the next section, validations of these concepts are shown using simulations.

4. Simulations

We consider an illumination wavelength of $\lambda = 475$ nm, and a NA = 1.4 microscope objective for detection. In order to mimic experimental conditions, we chose a fiber with a core refractive index of $n_{co} = 1.45$ with a diameter of $1 \mu\text{m}$ and a cladding of $n_{cl} = 1.43$ of diameter $5 \mu\text{m}$, $10 \mu\text{m}$ long, immersed in oil with a matching refractive index of $n_{im} = 1.51$, and illuminated perpendicularly to the rotation axis.

4.1. 3D reconstructions

4.1.1. DHM reconstruction

Simulation of the holographic acquisition process can be realized by applying a mask, corresponding to the accessible frequency content, onto the Fourier transform of the object. The mask corresponding to a holographic experiment is depicted Fig. 4(a), limited to a 2D cut for the sake of simplicity. As we are here working in 2D only, the cap of sphere is actually limited to a circular arc. Our method, shown Fig. 4(b), aims at filling the Fourier space by digitally rotating the frequency support. The effect on Fourier space is illustrated Fig. 4(c) for nine rotation angles: the Fourier space is better mapped, anticipating a better object reconstruction. Hence, one can easily improve image quality considering more angles in the reconstruction process. **Images were obtained by first performing a 3D-FFT on our simulated object. Then, considering the first Born approximation, a product is made between and the object spectrum and the theoretical OTF using experimental conditions, i.e. numerical aperture, illumination wavelength, objectives immersion**

medium, magnification and CMOS pixel size. This step mimics the backpropagation approach, which is mandatory in order to take into account the diffraction phenomena. A comparison with the (filtered-)backprojection algorithm has been discussed by Gorski *et al.* [46], concluding filtered-backprojection is not as accurate as backpropagation when the diffraction phenomena is taken into account. Finally, an inverse 3D-FFT is performed to retrieve the diffracted field.

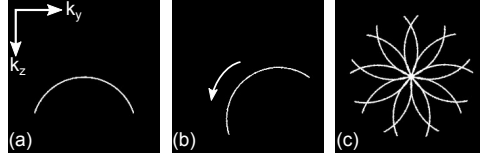


Fig. 4: (a) Accessible information in 2D Fourier space for DHM. (b) Digital rotation of the holographic circular arc. (c) Final frequency support merging nine digital rotations.

Results using both FINER and DINER reconstruction methods are displayed Fig. 5. Note that we used a special lookup-table that emphasizes artifacts. As expected by the theory, reconstruction in the DHM case shows very poor resolution in the three x , y and z directions due to its limited bandwidth (Fig. 5(a)) compared to ground truth shown Fig. 5(c),(g). It can also be noticed in Fig. 5(k),(l) a poor quantitative restitution of the refractive index of the cladding around 1.49.

For FINER and DINER reconstructions (Fig. 5(e),(i) and (f),(j) respectively), resolution is closer to that of the simulated object thanks to the frequency spectrum enlargement seen in Fig. 5(b). Contrary to the DHM case, a resolution improvement is clearly visible along the z axis, as well as a perfectly circular shape of the fiber. Quantitatively, it also better matches the expected values of core and cladding of the fiber. In order to discriminate quality reconstruction of both methods, mean squared error has been calculated: the FINER approach leads to a MSE of 3.3×10^{-5} while the DINER one leads to 4.3×10^{-5} . Furthermore, while FINER uses only two 3D-FFT (one at the beginning and one at the end to reconstruct the object after the rotation process), DINER uses $2N$ 3D-FFT for N rotation angles (one forward to get the spectrum and one backward to reconstruct the object for each angle). Hence, the FINER approach is more appropriate for that task, being more accurate and faster than the DINER method. However, one can see large oscillations in the fiber and in the immersion medium: this is an effect of the “missing apple core”, which is discussed in section 2.

Thus, a simple numerical rotation of a DHM image might not be enough to reconstruct smaller objects or sharp edges. For that purpose, *i.e.* retrieving higher frequencies as well as frequencies in the so-called “missing apple core” [38], we propose to apply DINER and TINER techniques to TDM with illumination rotation images.

4.1.2. TDM reconstructions

If one wants to reconstruct the sample more precisely than with FINER/DINER methods, TDM images can be used as a basis in the rotation process. In that case, a prior illumination rotation has to be performed so as to record the typical OTF shape seen in Fig. 2(b). Reconstruction results in this configuration with corresponding Fourier space sections (k_y-k_z) are shown in Fig. 6. Figs. 6(e),(j) represent the sagittal and transversal cuts of the simulated object, respectively. In order to compare the obtained results, we also show the reconstructions in DHM (Fig. 6(a),(f) and (k)) and with FINER method (Fig. 6(b),(g) and (l)).

Figs. 6(h),(m) show the reconstruction obtained in TDM with illumination rotation, and its corresponding spectrum Fig. 6(c). One can see the improved resolution along the x and y axes compared to Figs. 6(f),(k) due to the extended frequency spectrum along the respective k_x, k_y frequency axes. However, even with such a frequency filling, we can still notice a limited resolution due to the so-called “missing cone”, best seen in the sagittal view, which does not

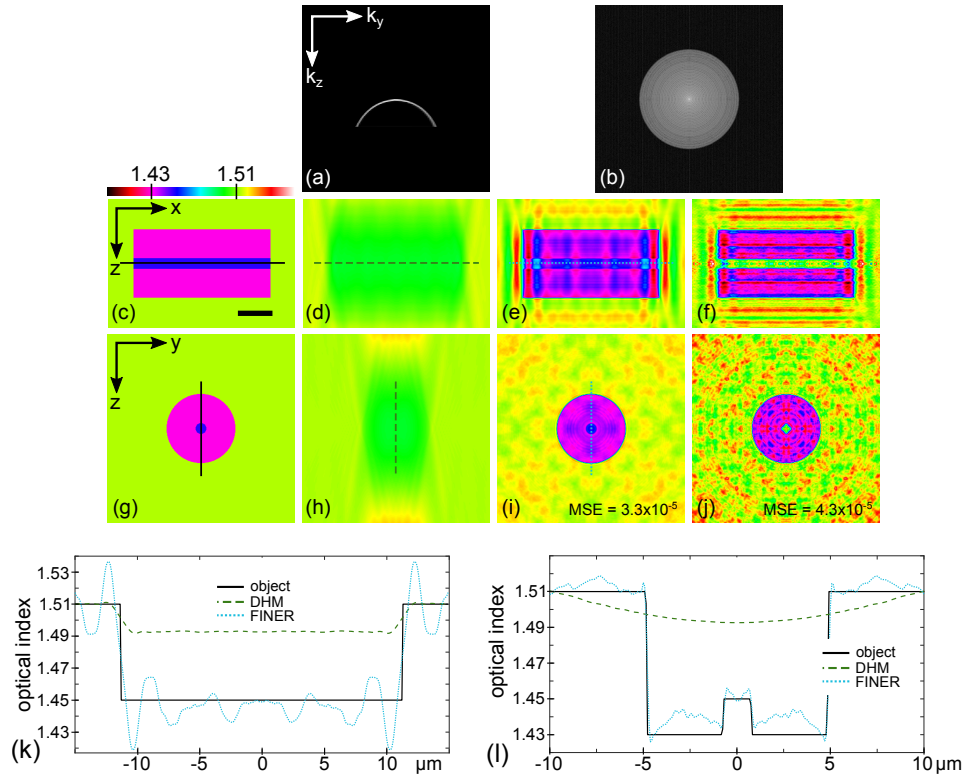


Fig. 5: Reconstruction of the simulated fiber in holography. (a) and (b) show the Fourier spectra corresponding to the images in the lower row. (c),(g) Simulated cylinder. (d),(h) Reconstruction in the DHM case. (e),(i) Reconstruction using FINER and (f),(j) DINER approach with 360 rotation angles. (k),(l) Profiles of (y-z) and (x-z) cross sections respectively. Color bar: real part of the refractive index. Scale bar: 2.5 μm .

show the circular shape of the fiber. One can assess reconstruction quality looking at the plotted profiles in Figs 6(o),(p). Even if TDM does not show oscillations as large as with the FINER method, the three approaches display non fitting values of refractive indices due to their lost frequencies, coming from the very limited bandwidth (for DHM), the so-called “missing apple core” (for FINER) or “missing cone” (for TDM). Figs. 6(i),(n) display the reconstruction images obtained using F-TINER approach for two rotation angles (0° and 90°). The corresponding spectrum in Fig. 6(d) shows an identical space filling along the three perpendicular directions k_x , k_y and k_z . A clear resolution improvement can also be seen, especially in the sagittal view, displaying an almost perfectly circular shape of the cylinder contrary to a single illumination rotation reconstruction. Also, the exact values of 1.45 and 1.43 for the average cladding and core optical indexes are retrieved.

Another example of application of the proposed methods is presented in Fig. 7, comparing reconstructions with FINER, illumination rotation and F-TINER methods (from left to right). The sample (Fig. 7(a)) consists of a bead attached to an optical fiber [47]. While Fig. 7(b) displays a good resolution in x direction as in Fig. 7(c), it shows a lack of resolution along the y axis, compared to the illumination rotation method. Also, one can notice oscillations in the x direction due to the “missing apple core” effect as discussed in the previous sections. Finally, a numerical

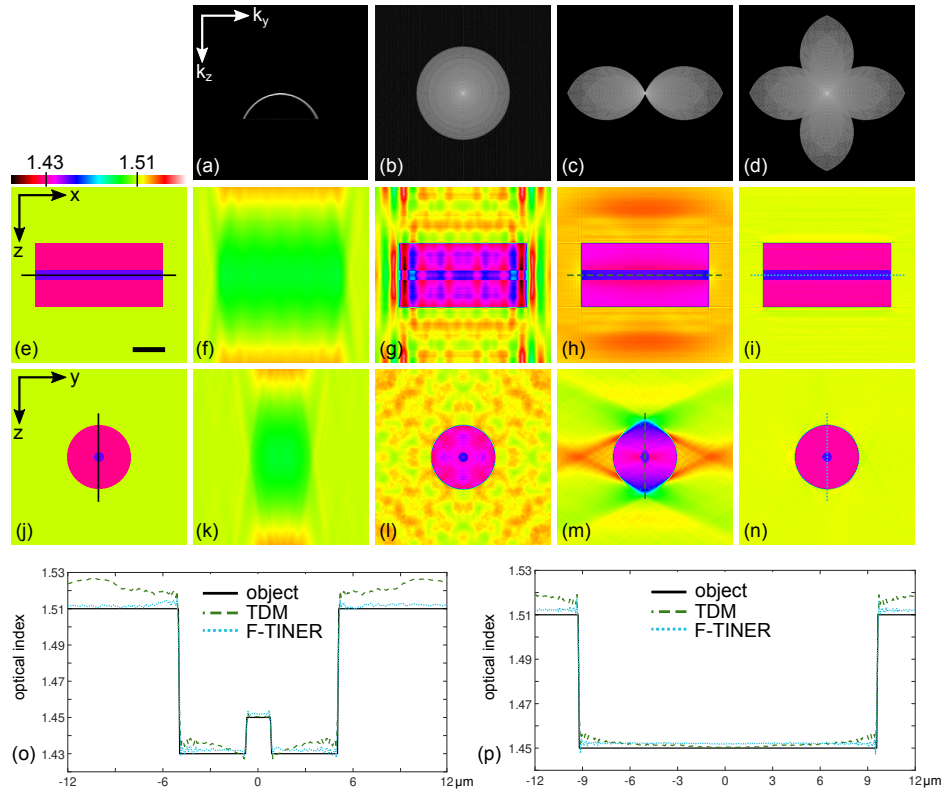


Fig. 6: Reconstruction of the simulated fiber in tomography. (a)–(d) show the Fourier spectra corresponding to the images in the lower row. (e),(j) Simulated cylinder. (f),(k) Reconstruction in DHM. (g),(i) Reconstruction using FINER method. (h),(m) Reconstruction in TDM with illumination rotation (600 angles). (i),(n) Reconstruction using F-TINER approach with two rotation angles (0° and 90°). (o),(p) Profiles of (x – y) and (x – z) cross sections respectively. Color bar: real part of the refractive index. Scale bar: $2.5 \mu\text{m}$.

rotation with F-TINER (Fig. 7(d)) allows for an excellent reconstruction, both in terms of shape and refractive index homogeneity.

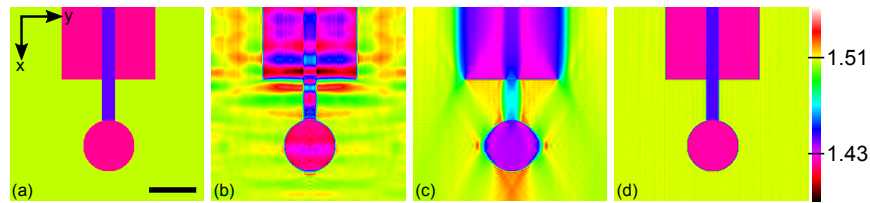


Fig. 7: Reconstruction of a simulated bead attached to an optical fiber. (a) Simulated object. (b) FINER method. (c) TDM with illumination rotation. (d) F-TINER method. Scale bar: $2.5 \mu\text{m}$.

4.1.3. Number of acquisitions leveraging

A drawback of TDM is the necessity to acquire many views. An advantage of the proposed methods is that Fourier space filling is also performed numerically, which can compensate lower filling by physical acquisitions. To illustrate this feature, we investigate whether it is better to have a lot of illumination angles and a few numerical rotation of data, or a few illumination angles and a lot of numerical rotation of data. Hence, we compared two cases, both based on a total of 600 angles: the first one is with 300 illumination angles and only 2 numerical rotations of data, the second one with 100 illumination angles and 6 numerical rotations of data. Results are shown in Fig. 8.

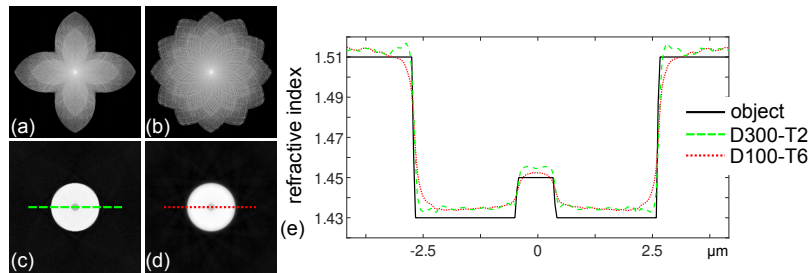


Fig. 8: Top row: Fourier space. Bottom row: sagittal cut. (a),(c) D300-T2: 300 illumination angles donut-shaped spectrum numerically rotated twice using F-TINER method. (b),(d) D100-T6. (e) Plotted profiles. Scale bar: 2.5 μm .

The first case results (called D300-T2) are displayed Fig. 8(a) for the spectrum spectrum and Fig. 8(c) for the corresponding sample reconstruction. Figure 8(b) depicts the spectrum obtained with the second case (called D100-T6), for 100 illumination angles, which would correspond to a speed-up of a factor 3 in the acquisition process, compensated by 6 F-TINER rotations, only limited by computer speed. Figure 8(e) shows reconstruction profiles: despite strong decrease in the quantity of original TDM data, final reconstructions are of almost same accuracy. One could even further decrease the number of acquisitions if using more elaborate iterative reconstruction methods, but those, as Abel inversion, often make restrictive assumptions such as non-absorbing samples, or involve positivity constraints [48]. These results show that F-TINER can also help decreasing the number of acquisitions necessary for precise image reconstructions, but such optimizations are often specimen-dependent, so would require detailed-, case-by-case investigations.

4.2. Robustness

In this section, we study the robustness of the numerical rotation, considering first the effect of noise on the reconstructions, then the case of an inclusion in the sample.

4.2.1. Noise influence

For this study, we examine the effect of noise only on a sagittal view of the sample. In that case, we only consider phase noise one would have obtain with a DHM acquisition. Other noise sources like speckle noise or shot noise are not relevant for our system because of their respective origins:

- a) speckle noise depends on the beam apparent angle on the sample and the illumination wavelength. In our setup, as we work with a 475 nm laser source and a x120 magnification system, the speckle grain size appears to be bigger than the field of view (about $45 \mu\text{m} \times 45 \mu\text{m}$);

b) a strong advantage of TDM is that one can work with strong signals and high dynamics, contrary to other microscopy imaging modalities (fluorescence for example). As a consequence, shot noise does not need to be considered in our tomographic setup. As a matter of fact, its effect is well below that of the other noise sources.

We first apply a white Gaussian noise with a standard deviation σ of 10% of the minimal index variation of the object, *i.e.* between the core (optical index 1.45) and the cladding (1.43): $\sigma = \Delta n_{\min} \times 10\% = 0.002$ (Fig. 9(a)). This noisy image, for a given standard deviation, is used as a basis for every following reconstructions, as theoretically only one holographic acquisition is performed. Hence, even with a limited bandwidth, all the frequencies are equally affected by the white noise. Then, both Fourier and DHM image rotations are performed, which results are displayed in Figs. 9(b) and 9(c). Respective profiles are plotted in Fig. 9(d). Both reconstruction methods show good results, being robust to noise. This can be explained as follow: numerically rotating and merging of the data induces circular arcs to overlap in Fourier space (see Fig. 4(c)), generating frequency redundancy; information is then averaged, reducing the noise effect on the reconstructions.

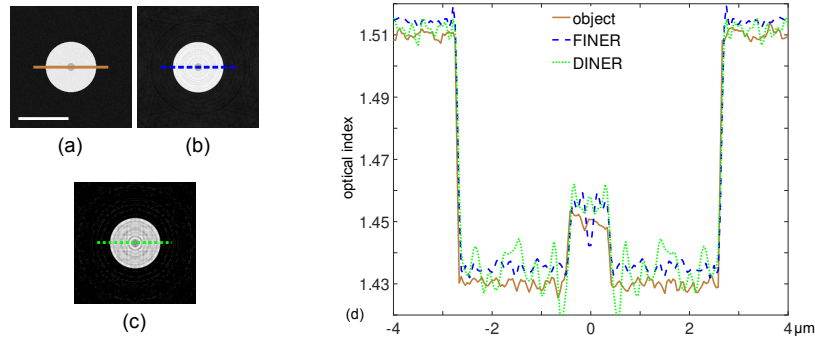


Fig. 9: Noise effect on reconstructions. (a) Cylinder with white Gaussian noise of $\sigma = 10\%$ of the global value range. Reconstructions using (b) FINER and (c) DINER methods for 360 angles of rotation. (d) Respective profiles. Scale bar: $5\ \mu\text{m}$.

In order to obtain a more quantitative information of the effect of noise in the reconstructed images, we investigated the signal-to-noise ratio (SNR) as a function of the number of rotation angles. For this purpose, six different Gaussian noise levels are applied on the simulated object, defined by their standard deviation in percentage of minimum range value, going from 1% to 30% of Δn_{\min} . Then, a DHM image is generated, which serves as a basis: for every number of rotation angles, reconstructions are obtained by rotation of the DHM image in Fourier space as with the FINER method. Results are depicted Fig. 10 in decibels, in logarithmic scale.

One can see two parts in the SNR graph. The first part, going from 1 (DHM) to 10 rotation angles, shows a decreasing function: this might come from the low number of rotated caps of sphere, which does not allow for a proper frequency averaging. The second part, starting from about 10 rotation angles and displaying an increasing SNR, shows that, in order to have a SNR close to DHM reconstruction one, at least 45 rotation angles are necessary. For 180 angles, SNR for a $\sigma = 5\%$ rises up to 61 dB whereas it is only at 55 dB for $\sigma = 30\%$. Also, one can notice that the more reconstruction angles are considered, the higher the SNR (at least until 180 rotation angles), thanks to the averaging of frequencies in Fourier space. For example, for a standard deviation of $\sigma = 10\%$ and 180 rotation angles, SNR stands at 60 dB, while for 10 angles it is around 47 dB.

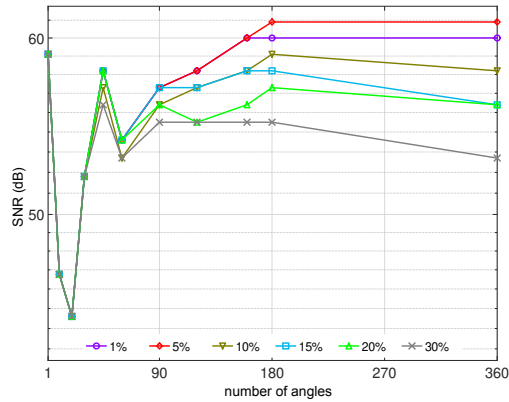


Fig. 10: Logarithmic representation of SNR in dB as a function of the number of rotation angles for different values of standard deviation.

4.2.2. Reconstruction with inclusions

In order to test the numerical rotation robustness onto more realistic samples, we added a defect in the simulated object, consisting in an inclusion of 500 nm and of optical index 1.51, like the immersion medium index. Results using both FINER and DINER methods are displayed Fig. 11.

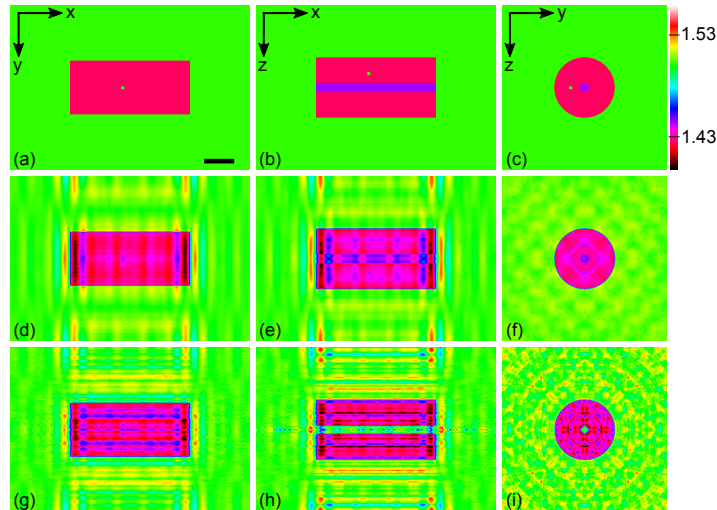


Fig. 11: Reconstruction of the sample presenting a defect of refractive index 1.51. (a)–(c) Simulated object. (d)–(f) Reconstruction with FINER approach. (g)–(i) Reconstruction with DINER approach. Color bar: refractive index. Scale bar: 2.5 μm .

For both reconstruction approaches, the inclusion is smeared out as an annular structure around the fiber core, with a diameter corresponding to the initial distance between the defect and the core, as expected from the proposed methods, which consist in rotating available data. However, the inclusion is less visible with both methods. It can be explained by two factors:

- not all inclusion frequencies might have been recorded when simulating a DHM acquisition due to the limited numerical aperture of the objectives;

- the frequency averaging in the Fourier space, as already observed with the noise effect in the previous part, which smears out the defect.

The main drawback of this technique is inherent to the numerical rotation itself: if a defect is too big compared to the initial sample, it will be considered as a distinct object. As we rotate the information, it will therefore propagate over the whole space, leading to an incorrect reconstruction. If needed, this could be counteracted using *a priori* information on the sample or inpainting techniques [49], but also indicates that such larger defects could be detected as unexpected structures, then triggering a more detailed investigation, with physical rotation of the sample, as in [18].

In conclusion, we showed the proposed methods are robust to strong noise and strongly diffracting small defects, especially with the FINER approach, which is an advantage in diffraction tomography compared to other methods such as Abel inverse transform.

5. Application to experimental data

In order to validate the proposed approach for practical cases, we apply the numerical reconstruction to experimental data. For this purpose a stretched optical fiber is used, having a very sharp tip of about 1 μm long on one end (obtained by the heat-and-pull technique [50], which can produce tips with end diameter of less than 100 nm [18]). It is illuminated by a 475 nm wavelength laser, and the diffracted field is collected using a $\times 100$ magnification and 1.4 numerical aperture oil immersion objective. Reconstructions are made in the Rytov approximation [51]. A stepper motor controls the rotation of the specimen. Results are displayed Fig. 12.

Figures 12(a)–(f) show lateral (x – y), axial (x – z) and sagittal (y – z) planes of the optical fiber obtained in illumination rotation TDM with no sample rotation and with a 4-angles specimen rotation respectively (0° , 54° , 90° and 126° – for more details about data acquisition, see [18]). The estimated resolution in Fig. 12(a) is 95 nm in (x – y) plane for a single TDM acquisition. After four TDM data registration, the obtained resolution is almost isotropic, at 150 nm in (x – y) plane and 180 nm in (x – z) plane, thanks to the better filling of the Fourier space [18]. This improvement allows to see the tip of the fiber indicated with a white arrow. The difference in resolutions is due to residual mismatches during the registration process, which is not perfect. This effect, combined with the limited number of angles used for the reconstruction, can be seen in the sagittal view where the shape of the fiber is not perfectly circular.

In Figs. 12(g)–(i) are shown the reconstructions using the numerical rotation of data, as in the TNER method, with the same 4 angles. One can see a dramatic improvement in image quality in both (x – y) and (x – z) planes. But contrary to physical rotation of the sample, our method easily allows for considering more rotations, providing better reconstruction, as can be seen in Figs. 12(j)–(l), displaying the reconstructed object using 20 rotation angles. The fiber is now reconstructed as circular (Fig. 12(l)). Finally, reconstruction quality can be assessed by looking at the normalized optical index shown in Fig. 12(m). A higher number of rotation angles allows for a better reconstruction, closer to the expected values if a physical rotation of the fiber was made, compared to TDM with no sample rotation.

However, one can see residual artifacts in the middle of the fiber of Figs. 12(g), (h), (j) and (k), depicted by a double red arrow. For our sample, it coincides with the fiber tip, which image is then degraded. This noise artifact is common in TDM, while it does not occur in other tomographic imaging fields. When considering full TDM acquisition with illumination scanning, artifacts present in the reference beam arm are coherently summed for each acquired image. This lead to a very noisy plane at the center of the reconstructed volume. This effect has been pointed out by Kostencka [52]. Moreover, in a classical TDM acquisition the imaged object is brought into focus prior recording (this step is mandatory to maintain the acquisition resolution). Thus, the central plane of the reconstructed object coincides with the noisy plane. One solution is to slightly defocus the object before the acquisition and the object’s image is then numerically brought back

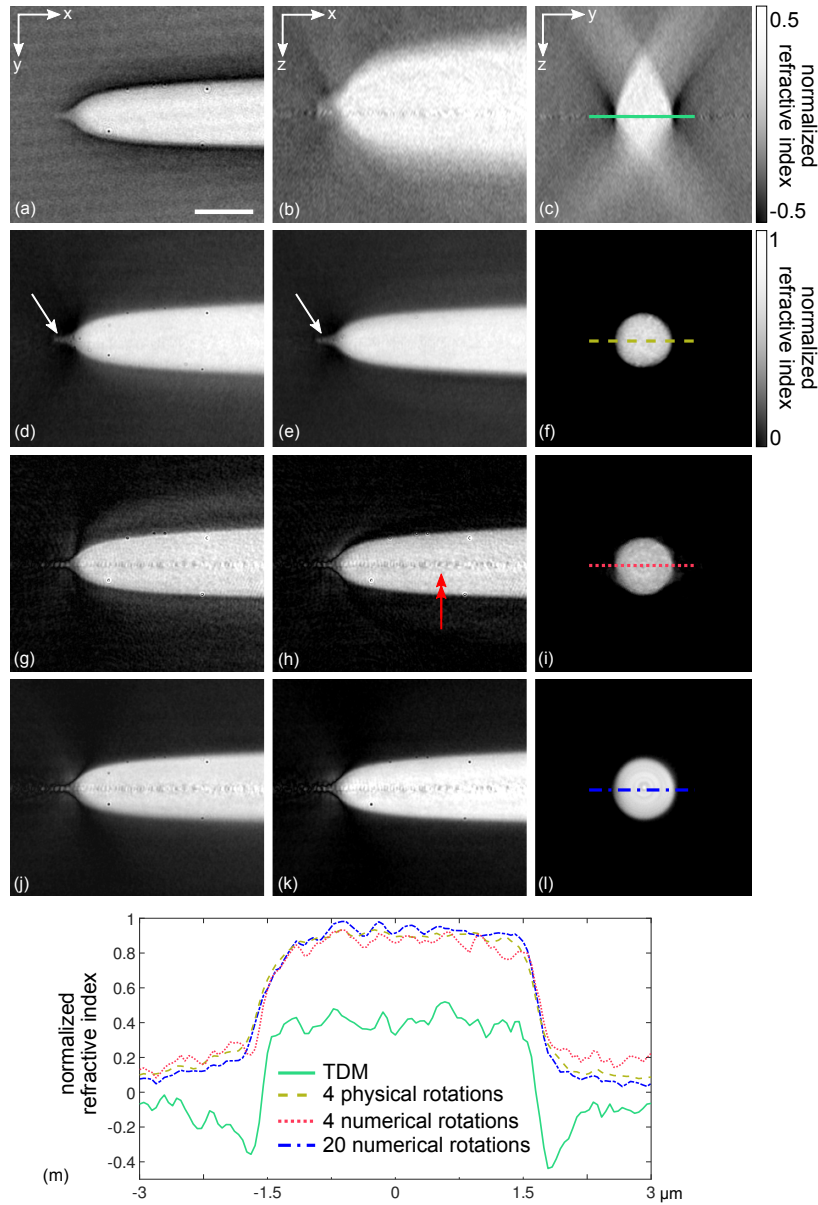


Fig. 12: Lateral (left), axial (center) and sagittal (right) views of a stretched optical fiber reconstructed in the Rytov approximation using TDM. (a)–(c) Reconstruction in TDM with illumination rotation without sample rotation. (d)–(f) 4-angles physical rotation (0° , 54° , 90° and 126°). (g)–(i) 4-angles numerical rotation with the same 4 angles using TINER method. (j)–(l) 20-angles numerical rotation. (m) Plotted profiles. Scale bar: $3 \mu\text{m}$.

to focus in the reconstruction. The same effect is noticeable with our method. However, as we rotate one tomographic acquisition, this noisy plane becomes a noisy line, corresponding to the symmetry axis of the sample. Two solutions can be found to this problem. As above, starting with a defocused acquisition, and alternately, as only a single line is corrupted by this noise, one could remove it by image processing approaches. This effect is clearly detrimental on the

reconstruction of the microtip at the end of the tapered fiber, which is better seen Figs. 12(d),(e) (physical rotation of the fiber) than on Figs. 12(j),(k) (numerical rotation of data). This is however a very specific drawback of our sample, which smallest structure coincides with the axis of symmetry. On the contrary, the advantage of our approach clearly appears when measuring the global shape of the object, which is much better reconstructed, as seen in Fig. 12(m).

6. Conclusion

We propose four reconstruction methods in TDM, applicable to specific samples exhibiting cylindrical symmetry. These approaches allow for a simplification of the acquisition process and a reduction of the acquisition time. Compared to the Abel inverse transform, our methods takes into account diffraction. For cylindrical samples (invariant along the rotation axis), we show the feasibility of the numerical rotation of an holographic spectrum in Fourier space, or by rotating the holographic image recorded with a conventional DHM. However, this method is less efficient for axisymmetric samples (not invariant along the rotation axis) because of the “missing apple core” present in the OTF recorded in TDM with sample rotation. For such objects, one has to proceed to one TDM acquisition with illumination rotation first, in order to have a good resolution along the rotation axis. Then this spectrum is numerically rotated so as to enhance resolution along the optical axis. We show this last method to work on both simulated and experimental data.

This approach could have applications to study various natural (for example spider silk fibers [53]) as well as artificial samples (functionalized nano/microfibers [54], Taylor cones and cone jet bridges [55,56], textile fibers, 3D imaging of glass micro-capillary [57], nanopipettes [58], droplets levitation [59] and spreading [60], and polymer fiber tip fabrication [47,61]). Indeed, for spherical samples such as droplets or cylindrical samples such as fibers, inverse problem approaches deliver unsurpassed results in terms of measurements’ accuracy [62,63]. They are however often used to precise determination of few parameters about the sample (its diameter for example), while making very strong assumptions about its shape (spherical, cylindrical, ellipsoidal), and its index of refraction (usually being homogeneous). Our approach is less precise in terms of measurements’ accuracy, but leverage hypotheses about the sample, only assuming axisymmetry. But our techniques could also be used in conjunction with inverse problem approaches in holography [64] and tomography [65,66], to further improve image quality, and also has the advantage that it could be readily used by interested readers, wether willing to develop their own DHM/TDM microscopes, or using commercially available ones.

Acknowledgments

We acknowledge financial support from Région Grand Est for Ludovic Foucault PhD fellowship under grant n° 544/15/C13 and Agence Nationale de la Recherche (ANR) (ANR-11-JS10-0003 OSIRIS). We thank both anonymous reviewers for their helpful remarks and comments to improve the paper.

References

1. K. Nenadic, I. Novak, J. Job, F. Jovic, and Z. Jagnjic, “A Possibility of Applying Differential Digital Holography in Manufacturing Process,” in *Proceedings ELMAR 2006*, (IEEE, Zadar, 2006).
2. A. Simic, H. Freiheit, M. Agour, C. Falldorf, and R. B. Bergmann, “In-line quality control of micro parts using digital holography,” in *Proceedings SPIE 10233*, (SPIE, Prague, 2017).
3. N. Gisin, R. Passy, and B. Perny, “Optical fiber characterization by simultaneous measurement of the transmitted and refracted near field,” *J. Light. Technol.* **11**, 1875–1883 (1993).
4. T. C. Wedberg and W. C. Wedberg, “Tomographic reconstruction of the cross-sectional refractive index distribution in semi-transparent, birefringent fibres,” *J. Microsc.* **177**, 53–67 (1995).
5. M. Young, “Mode-field diameter of single-mode optical fiber by far-field scanning,” *Appl. Opt.* **37**, 5605–5619 (1998).

6. X. Buet, C. Brun, J. Gâteau, B. Bresson, S. R. Sandoghchi, E. N. Fokoua, M. Petrovich, F. Poletti, D. Richardson, D. Vandembroucq, and G. Tessier, "Nondestructive measurement of the roughness of the inner surface of hollow core-photonic bandgap fibers," *Opt. Lett.* **41**, 5086–5089 (2016).
7. M. Malek, H. Khelifa, P. Picart, D. Mounier, and C. Poilâne, "Microtomography imaging of an isolated plant fiber: a digital holographic approach," *Appl. Opt.* **55**, A111–A121 (2016).
8. Y. Bao and T. K. Gaylord, "Iterative optimization in tomographic deconvolution phase microscopy," *J. Opt. Soc. Am. A* **35**, 652–660 (2018).
9. T. Sokkar, K. El-Farahaty, W. Ramadan, H. Wahba, M. Raslan, and A. Hamza, "Nonray-tracing determination of the 3d refractive index profile of polymeric fibres using single-frame computed tomography and digital holographic interferometric technique," *J. Microsc.* **257**, 208–216 (2015).
10. M. H. Jenkins and T. K. Gaylord, "Three-dimensional quantitative phase imaging via tomographic deconvolution phase microscopy," *Appl. Opt.* **54**, 9213–9227 (2015).
11. B. Kemper, S. Kosmeier, P. Langehanenberg, G. von Bally, I. Bredebusch, W. Domschke, and J. Schneckeburger, "Integral refractive index determination of living suspension cells by multifocus digital holographic phase contrast microscopy," *J. Biomed. Opt.* **12**, 054009 (2007).
12. L. Martínez-León and B. Javidi, "Synthetic aperture single-exposure on-axis digital holography," *Opt. Express* **16**, 161–169 (2008).
13. M. Debailleul, V. Georges, B. Simon, R. Morin, and O. Haeberlé, "High-resolution three-dimensional tomographic diffractive microscopy of transparent inorganic and biological samples," *Opt. Lett.* **34**, 79–81 (2009).
14. R. Fiolka, K. Wicker, R. Heintzmann, and A. Stemmer, "Simplified approach to diffraction tomography in optical microscopy," *Opt. Express* **17**, 12407–12417 (2009).
15. Y. Cotte, F. Toy, P. Jourdain, N. Pavillon, D. Boss, P. Magistretti, P. Marquet, and C. Depeursinge, "Marker-free phase nanoscopy," *Nat. Photonics* **7**, 113–117 (2013).
16. T. D. Yang, H.-J. Kim, K. J. Lee, B.-M. Kim, and Y. Choi, "Single-shot and phase-shifting digital holographic microscopy using a 2-D grating," *Opt. Express* **24**, 9480–9488 (2016).
17. J. Li, Q. Chen, J. Zhang, Z. Zhang, Y. Zhang, and C. Zuo, "Optical diffraction tomography microscopy with transport of intensity equation using a light-emitting diode array," *Opt. Lasers Eng.* **95**, 26–34 (2017).
18. B. Simon, M. Debailleul, M. Houkal, C. Ecoffet, J. Bailleul, J. Lambert, A. Spangenberg, H. Liu, O. Soppera, and O. Haeberlé, "Tomographic diffractive microscopy with isotropic resolution," *Optica* **4**, 460–463 (2017).
19. U. Schnars and W. P. O. Jüptner, "Digital recording and numerical reconstruction of holograms," *Meas. Sci. Technol.* **13**, R85–R101 (2002).
20. N. Verrier and M. Atlan, "Off-axis digital hologram reconstruction: some practical considerations," *Appl. Opt.* **50**, H136–H146 (2011).
21. M. Debailleul, B. Simon, V. Georges, O. Haeberlé, and V. Lauer, "Holographic microscopy and diffractive microtomography of transparent samples," *Meas. Sci. Technol.* **19**, 074009 (2008).
22. W. Choi, C. Fang-Yen, K. Badizadegan, S. Oh, N. Lue, R. R. Dasari, and M. S. Feld, "Tomographic phase microscopy," *Nat. Methods* **4**, 717–719 (2007).
23. K. Lee, K. Kim, J. Jung, J. Heo, S. Cho, S. Lee, G. Chang, Y. Jo, H. Park, and Y. Park, "Quantitative Phase Imaging Techniques for the Study of Cell Pathophysiology: From Principles to Applications," *Sensors* **13**, 4170–4191 (2013).
24. M. Habaza, B. Gilboa, Y. Roichman, and N. T. Shaked, "Tomographic phase microscopy with 180° rotation of live cells in suspension by holographic optical tweezers," *Opt. Lett.* **40**, 1881–1884 (2015).
25. Y. Park, C. Depeursinge, and G. Popescu, "Quantitative phase imaging in biomedicine," *Nat. Photonics* **12**, 578–589 (2018).
26. S. Vertu, J. Flügge, J.-J. Delaunay, and O. Haeberlé, "Improved and isotropic resolution in tomographic diffractive microscopy combining sample and illumination rotation," *Cent. Eur. J. Phys.* **9**, 969–974 (2011).
27. T. Fukuda, Y. Wang, P. Xia, Y. Awatsuji, T. Kakue, K. Nishio, and O. Matoba, "Three-dimensional imaging of distribution of refractive index by parallel phase-shifting digital holography using Abel inversion," *Opt. Express* **25**, 18066–18071 (2017).
28. N. Abel, "Auflösung einer mechanischen Aufgabe," *J. für die reine und angewandte Math. (Crelles Journal)* pp. 153–157 (1826).
29. J. Bailleul, B. Simon, M. Debailleul, L. Foucault, N. Verrier, and O. Haeberlé, "Tomographic diffractive microscopy: Towards high-resolution 3-D real-time data acquisition, image reconstruction and display of unlabeled samples," *Opt. Commun.* **422**, 28–37 (2018).
30. E. Cucho, P. Marquet, and C. Depeursinge, "Spatial filtering for zero-order and twin-image elimination in digital off-axis holography," *Appl. Opt.* **39**, 4070–4075 (2000).
31. I. Yamaguchi and T. Zhang, "Phase-shifting digital holography," *Opt. Lett.* **22**, 1268–1270 (1997).
32. M. Atlan, M. Gross, and E. Absil, "Accurate phase-shifting digital interferometry," *Opt. Lett.* **32**, 1456–1458 (2007).
33. E. N. Leith and J. Upatnieks, "Reconstructed Wavefronts and Communication Theory," *J. Opt. Soc. Am.* **52**, 1123–1130 (1962).
34. M. Born and E. Wolf, *Principles of optics - Electromagnetic theory of propagation, interference and diffraction of light* (Cambridge University Press, 1999), 7th ed.
35. E. Wolf, "Three-dimensional structure determination of semi-transparent objects from holographic data," *Opt. Commun.* **1**, 153–156 (1969).

36. O. Haeberlé, K. Belkebir, H. Giovaninni, and A. Sentenac, "Tomographic diffractive microscopy: basics, techniques and perspectives," *J. Mod. Opt.* **57**, 686–699 (2010).
37. V. Lauer, "New approach to optical diffraction tomography yielding a vector equation of diffraction tomography and a novel tomographic microscope," *J. Microsc.* **205**, 165–176 (2002).
38. S. Vertu, J.-J. Delaunay, I. Yamada, and O. Haeberlé, "Diffraction microtomography with sample rotation: influence of a missing apple core in the recorded frequency space," *Cent. Eur. J. Phys.* **7**, 22–31 (2009).
39. A. Kus, M. Dudek, B. Kemper, M. Kujawska, and A. Vollmer, "Tomographic phase microscopy of living three-dimensional cell cultures," *J. Biomed. Opt.* **19**, 046009 (2014).
40. B. Vinoth, X.-J. Lai, Y.-C. Lin, H.-Y. Tu, and C.-J. Cheng, "Integrated dual-tomography for refractive index analysis of free-floating single living cell with isotropic superresolution," *Sci. Reports* **8**, 5943 (2018).
41. C. Wei, D. I. Pineda, C. S. Goldenstein, and R. M. Spearrin, "Tomographic laser absorption imaging of combustion species and temperature in the mid-wave infrared," *Opt. Express* **26**, 20944–20951 (2018).
42. C. M. Vest, "Interferometry of strongly refracting axisymmetric phase objects," *Appl. Opt.* **14**, 1601–1606 (1975).
43. Z. Pan, S. Li, and J. Zhong, "Digital holographic microtomography for geometric parameter measurement of optical fiber," *Opt. Eng.* **52**, 035801 (2013).
44. J. W. Goodman, *Introduction to Fourier optics* (W.H. Freeman, Macmillan Learning, New York, 2017), 4th ed.
45. A. T. Vouldis, C. N. Kechribaris, T. A. Maniatis, K. S. Nikita, and N. K. Uzunoglu, "Investigating the enhancement of three-dimensional diffraction tomography by using multiple illumination planes," *J. Opt. Soc. Am. A* **22**, 1251–1262 (2005).
46. W. Gorski and W. Osten, "Tomographic imaging of photonic crystal fibers," *Opt. Lett.* **32**, 1977–1979 (2007).
47. S. Jradi, O. Soppera, D. J. Lougnot, R. Bachelot, and P. Royer, "Tailoring the geometry of polymer tips on the end of optical fibers via control of physico-chemical parameters," *Opt. Mater.* **31**, 640–646 (2009).
48. K. Kim, K. S. Kim, H. Park, J. C. Ye, and Y. Park, "Real-time visualization of 3-D dynamic microscopic objects using optical diffraction tomography," *Opt. Express* **21**, 32269–32278 (2013).
49. H. Xia, S. Montessoro, R. Guo, J. Li, F. Olchewsky, J.-M. Desse, and P. Picart, "Robust processing of phase dislocations based on combined unwrapping and inpainting approaches," *Opt. Lett.* **42**, 322–325 (2017).
50. M. Xiao, J. Nieto, J. Siqueiros, and R. Machorro, "Simple device for making optical fiber tips for scanning near field optical microscopes," *Rev. Sci. Instruments* **68**, 2787–2789 (1997).
51. S. Caorsi, A. Massa, and M. Pastorino, "Rytov approximation: application to scattering by two-dimensional weakly nonlinear dielectrics," *J. Opt. Soc. Am. A* **13**, 509–516 (1996).
52. J. Kostencka, T. Kozacki, M. Dudek, and M. Kujawińska, "Noise suppressed optical diffraction tomography with autofocus correction," *Opt. Express* **22**, 5731–5745 (2014).
53. J. G. Hardy, L. M. Römer, and T. R. Scheibel, "Polymeric materials based on silk proteins," *Polymer* **49**, 4309–4327 (2008).
54. S. Ubaid, F. Liao, S. Linghu, J. Yu, and F. Gu, "Electrospun polymer bottle microresonators for stretchable single-mode lasing devices," *Opt. Lett.* **43**, 3128–3131 (2018).
55. I. G. Loscertales, "Micro/Nano Encapsulation via Electrified Coaxial Liquid Jets," *Science* **295**, 1695–1698 (2002).
56. F. Liu and C.-H. Chen, "Electrohydrodynamic cone-jet bridges: Stability diagram and operating modes," *J. Electrostat.* **72**, 330–335 (2014).
57. C. Macias-Romero, I. Nahalka, H. I. Okur, and S. Roke, "Optical imaging of surface chemistry and dynamics in confinement," *Science* **357**, 784–788 (2017).
58. S. Hennig, S. van de Linde, M. Lummer, M. Simonis, T. Huser, and M. Sauer, "Instant Live-Cell Super-Resolution Imaging of Cellular Structures by Nanoinjection of Fluorescent Probes," *Nano Lett.* **15**, 1374–1381 (2015).
59. V. Contreras, R. Valencia, J. Peralta, H. Sobral, M. A. Meneses-Nava, and H. Martinez, "Chemical elemental analysis of single acoustic-levitated water droplets by laser-induced breakdown spectroscopy," *Opt. Lett.* **43**, 2260–2263 (2018).
60. A. Eddi, K. G. Winkels, and J. H. Snoeijer, "Short time dynamics of viscous drop spreading," *Phys. Fluids* **25**, 013102 (2013).
61. R. Bachelot, C. Ecoffet, D. Deloeil, P. Royer, and D.-J. Lougnot, "Integration of micrometer-sized polymer elements at the end of optical fibers by free-radical photopolymerization," *Appl. Opt.* **40**, 5860–5871 (2001).
62. D. J. Little and D. M. Kane, "Subdiffraction-limited radius measurements of microcylinders using conventional bright-field optical microscopy," *Opt. Lett.* **39**, 5196–5199 (2014).
63. H. Liu, J. Bailleul, B. Simon, M. Debailleul, B. Colicchio, and O. Haeberlé, "Tomographic diffractive microscopy and multiview profilometry with flexible aberration correction," *Appl. Opt.* **53**, 748–755 (2014).
64. C. Fournier, F. Jolivet, L. Denis, N. Verrier, E. Thiebaut, C. Allier, and T. Fournel, "Pixel super-resolution in digital holography by regularized reconstruction," *Appl. Opt.* **56**, 69–77 (2017).
65. F. Momey, A. Berdeu, T. Bordy, J.-M. Dinten, F. K. Marcel, N. Picollet-D'hahan, X. Gidrol, and C. Allier, "Lensfree diffractive tomography for the imaging of 3d cell cultures," *Biomed. Opt. Express* **7**, 949–962 (2016).
66. A. Berdeu, F. Momey, B. Laperrousaz, T. Bordy, X. Gidrol, J.-M. Dinten, N. Picollet-D'hahan, and C. Allier, "Comparative study of fully three-dimensional reconstruction algorithms for lens-free microscopy," *Appl. Opt.* **56**, 3939–3951 (2017).